Numerical analysis of improvements to CO_2 injectivity in coal seams through stimulated fracture connection to the injection well

Min Chen[1], Lee J. Hosking[2]*, Richard J. Sandford[3], Hywel R. Thomas[1]

[1]Geoenvironmental Research Centre, School of Engineering, Cardiff University, Queen's Buildings, The Parade, Newport Road, CF24 3AA, Cardiff, UK

[2]Now at the Department of Civil and Environmental Engineering, Brunel University London, Kingston Lane, Uxbridge, Middlesex, UB8 3PH, UK

[3]Now at the Department of Geography and Environmental Management, University of the West of England, Frenchay Campus, Bristol, BS16 1QY, UK

*Corresponding author: Email: Lee.Hosking@brunel.ac.uk Tel: +44 (0) 1895 265376

Conflict of Interest: The authors declare that they have no conflict of interest

Abstract

This work presents a hybrid discrete fracture-dual porosity model of compressible fluid flow, adsorption and geomechanics during CO_2 sequestration in coal seams. An application of the model considers the influence of hydraulic fractures on CO_2 transport and the stress field of the coal. The low initial permeability of coal is compounded by the injectivity loss associated with adsorption-induced coal swelling, which is recognised as the major challenge limiting CO_2 sequestration in coal seams. In this model, the natural fracture network and coal matrix are described by a dual porosity model, and a discrete fracture model with lower-dimensional interface elements explicitly represents any hydraulic fractures. The two models are coupled using the principle of superposition for fluid continuity with a local enrichment approximation for displacement discontinuity occurring at the surface of hydraulic fractures. The Galerkin finite element method is used to solve the coupled governing equations, with the model being verified against analytical solutions and validated against experimental data. Simulation results show that the presence of a hydraulic fracture influences the distribution of gas pressure and improves the gas flow rate, as expected. The stress field of a coal seam is disturbed by CO_2 injection, especially the vertical stress, and the presence of a hydraulic fracture leads to a reduction in stress with permeability recovery starting earlier.

***Keywords*: Carbon sequestration; Hydraulic fracture; Adsorption; Coal swelling; Injectivity**

1. Introduction

Coal seams are considered viable formations for CO_2 sequestration, having gained increasing attention since the early 1990s by association with enhanced coal bed methane (ECBM) recovery. A number of field demonstration projects of CO_2 sequestration in coal have been conducted, including in China, USA, Canada, Japan, and Poland, as presented by Pan and Connell (2012) and Pan et al. (2018). These pilot tests have indicated that the decrease of coal seam permeability due to coal swelling is a key challenge limiting the future prospects of this sequestration option.

Successful injection of CO_2 into a coal seam requires an effective permeability to be sustained, which can often necessitate some form of permeability enhancement. A gas mixture may be injected instead of pure CO_2, however, N_2 flooding in the Ishikari Coal Basin, Japan, showed that the CO_2 injection rate was only temporarily boosted. Moreover, the permeability did not return to its initial value after CO_2 and N_2 were repeatedly injected, implying some degree of hysteresis (Fujioka et al., 2010). Instead, the stimulation of coal permeability by hydraulic fracturing has otherwise proven to be an effective way of improving CO_2 injection rates (e.g. van Bergen et al., 2009). Considering the aforementioned interactions between fluid flow, stress, temperature, and gas sorption, it remains important to improve our understanding of how exactly the induced fractures affect coal permeability evolution during CO_2 sequestration.

A pilot test indicated that swelling of coal upon CO_2 sorption may create a high stress zone, which forces the injection rates to drop significantly near the injection well (Fujioka et al., 2010). Clear bottomhole pressure build-up can also be observed, especially in low-permeability coal seams. These observations imply that gas flow in coal is highly coupled to the geomechanical behaviour. In order to understand the permeability evolution, it is necessary to account for the altered stress state of the coal, especially in the vicinity of injection wells.

Coupled stress and fluid flow in fractured porous media has been studied in depth in recent decades based on the fundamental work of Biot (1972) on the general theory of consolidation. The presence of a discrete fracture leads to a discontinuous displacement field, where displacement at one side of the fracture is not identical to that of the other side. As a result, continuum-based numerical methods, including the standard finite element method, the finite difference method, and the boundary element method, are not able to describe such discontinuous problems explicitly (Jing, 2003). Nevertheless, explicit representation of discontinuities with continuum-based numerical methods has been pursued. Some studies adopted the finite element method with interface elements to describe hydro-mechanical behaviour in deformable fractured porous media, whereby the fracture is treated as a zero-

thickness element, or Goodman's joint element (Goodman et al., 1968; Ng and Small, 1997). However, this approach requires the finite element mesh to coincide with fractures and complicates the meshing task, such as through the generation of zero-thickness interface elements with double nodes, which also has an adverse impact on computational efficiency. In recent decades, numerical methods that combine continuum-based and dis-continuum-based numerical methods have been developed, such as the combined finite-discrete element method (Munjiza, 2004; Mahabadi et al, 2012; Lisjak and Grasselli, 2014), which is used to simulate the process of transition from continua to dis-continua, although the computational cost is relatively high.

Another numerical method used to capture the effect of deformation across a fracture on fluid flow is an enrichment approximation, such as the extended finite element method. Unlike the standard finite element method, the extended finite element method is able to deal with discontinuities with the jump function independent of the mesh. This method has received much attention in recent years in simulating discontinuities (Mohammadnejad and Khoei, 2013; Réthoré et al., 2007; Salimzadeh and Khalili, 2015). Watanabe et al. (2012) presented a numerical method with a partial, modified adaptation of the extended finite element method to incorporate pre-existing fractures. Lower-dimensional interface elements represent the fractures and the local finite element enrichment approximation is adopted for a fracture relative displacement function. This method requires less dependencies of the mesh on finite element approximations for the displacement function compared with the conventional interface element method. In particular, the method allows for the use of a single mesh for both mechanical and other related processes such as fluid flow.

The purpose of this study is to investigate variations in the stress field of coal seams during CO_2 injection and determine the influence of hydraulic fractures. In order to accurately describe flow behaviour and the related mechanical processes, a hybrid model of fully coupled compressible fluid flow, adsorption and geomechanics is proposed as a combination of the dual porosity and discrete fracture models. The natural fracture network and porous coal matrix are described together by a dual porosity model, and the effect of hydraulic fractures is represented explicitly by a discrete fracture model with lower-dimensional interface elements. The interaction of the two models is solved by assuming flow continuity over the fracture continuum and hydraulic fractures, and by using the principle of superposition. The discontinuity in displacement across a discrete fracture is considered simultaneously with the local enrichment approximation at the fracture elements for a discontinuous displacement function. The numerical model is implemented in an existing coupled thermal, hydraulic, chemical, and mechanical (THCM) model, COMPASS, developed by Thomas and co-workers (Chen et al., 2019; Hosking et al., 2017; Masum and Thomas, 2018; Thomas and He, 1998). The developed numerical model is verified by using

analytical solutions as benchmarks. Finally, the model is applied to investigate the effects of a hydraulic fracture on the flow behaviour and stress field within a coal seam during CO_2 sequestration.

2. Mathematical model

Coal reservoirs have multi-scale fractures, including a uniformly distributed network of natural fractures, also called cleats, and sparse large-scale fractures. The cleat system consists of face cleats and butt cleats. The former are continuous throughout the reservoir and the latter are shorter and disconnected, normally being perpendicular to face cleats. Large-scale fractures may form naturally as faults or artificially as hydraulic fractures. In this work, a discrete fracture model is employed to describe the effect of large-scale fractures. The uniformly distributed fracture networks (composed of micro-fractures) and the coal matrix are modelled using a dual porosity approach. Fig. 1 shows the development process of the integrated dual continuum and discrete fracture model. This new numerical model comprises three different media: the matrix continuum (*m*), the fracture continuum (*f*), and the hydraulic fractures (*F*). Fig. 2 shows the transport regime in the different domains, whereby fluid firstly flows into hydraulic fractures from the wellbore and then spreads to the natural fracture network, subsequently leaking into the coal matrix.

In this section, a set of governing equations describing compressible fluid flow and mechanical behaviour is presented for flow in a fractured coal seam. The superscripts m, f and F denote the matrix, natural fractures and hydraulic fractures. The coupled model is constructed from four sub-models; two fluid flow models for the natural fracture and rock matrix continua, respectively, one fluid flow model for hydraulic fractures, and a poroelastic deformation model. There are three primary flow variables, namely, the gas concentrations in the fracture continuum (c_f), porous matrix continuum (c_m), and hydraulic fractures (c_F). The displacement vector ($\mathbf{u}$) is the primary variable for mechanical behaviour. The model is developed based on the following assumptions: (1) gas is free phase in both natural and hydraulic fractures; only gas in matrix pores may be adsorbed; (2) the rock matrix is homogenous and isotropic and deformation is linear elastic; (3) flows in the natural fracture continuum and hydraulic fractures obey Darcy's law and the cubic law, respectively; (4) coal is dry and isothermal; (5) hydraulic fractures are embedded in the fracture continuum and the gas concentration of a hydraulic fracture is equal to the concentration that the fracture system has on the two surfaces of the hydraulic fracture.

2.1 Gas storage in the matrix continuum

The governing equation for gas storage in the matrix continuum considers mass conservation with pseudo-steady state leakage, which is defined as a diffusive process and expressed as

$$\frac{\partial}{\partial t}[n_m c_m + c_s] = q_{sm} + q_{fm} \tag{1}$$

where n_m is the matrix continuum porosity, c_m is the concentration of free gas in the matrix, c_s is the adsorbed mass per unit volume, q_{sm} is the sink-source term in the matrix, and q_{fm} represents the leak-off flow between the fractures and matrix, written as

$$q_{fm} = D\Psi(c_f - c_m) \tag{2}$$

where c_f is the concentration of free gas in the fracture continuum, Ψ is a shape factor dependent on the coal matrix block geometry, and D is the gas diffusion coefficient. Generally, a diffusion time, $\tau = \frac{1}{D\Psi}$, is introduced to approximate diffusivity within the coal matrix (Peng et al., 2014).

The gas adsorption behaviour can generally be described by a Langmuir isotherm, as

$$c_s = \rho_s \frac{V_L u_m}{u_m + u_L} \tag{3}$$

where ρ_s is the coal density, V_L is the Langmuir volume, u_L is the Langmuir pressure, and u_m is the matrix gas pressure, expressed as

$$u_m = Z_m R T c_m \tag{4}$$

where R is the universal gas constant, T is the temperature, and Z_m is the compressibility factor in the matrix, which is calculated in this work using the Peng-Robinson equation of state (Peng and Robinson, 1976).

Substitution of equations (2)-(4) into the mass balance equation (1) yields

$$\left(n_m + \frac{\partial c_s}{\partial c_m}\right)\frac{\partial c_m}{\partial t} + c_m \frac{\partial n_m}{\partial t} = \frac{1}{\tau}(c_f - c_m) + q_{sm} \tag{5}$$

2.2 Gas flow in the fracture continuum

The governing equation for gas flow in the natural fracture network can be obtained by combining mass balance with Darcy's law, written as

$$\frac{\partial}{\partial t}(n_f c_f) = -\nabla \cdot (c_f \mathbf{v}_f) - q_{fm} + q_{fF} + q_{sf} \tag{6}$$

where n_f is the fracture continuum porosity, q_{sf} is the sink-source term in the fracture continuum, q_{fF} is the leak-off flow between the hydraulic and natural fractures, and $\mathbf{v}_f$ is the advective flow velocity. Ignoring gravity, $\mathbf{v}_f$ can be given as

$$\mathbf{v}_f = -\frac{k_f}{\mu_g}\nabla u_f \tag{7}$$

where k_f is the intrinsic permeability of the fracture continuum, μ_g is the gas viscosity, and $u_f = Z_m RT c_f$ is the gas pressure in the fracture continuum.

Combining equations (2), (6) and (7) and rearranging yields the final form of the governing equation for gas flow in the fracture continuum

$$n_f \frac{\partial c_f}{\partial t} + c_f \frac{\partial n_f}{\partial t} = -\nabla \cdot \left(c_f \frac{k_f}{\mu_g} Z_m RT \nabla c_f \right) - \frac{1}{\tau}\left(c_f - c_m\right) + q_{sf} + q_{fF} \tag{8}$$

2.3 Gas flow in hydraulic fractures

A separate flow model is developed for discontinuities using the discrete fracture approach. Discrete fractures are treated as lower dimensional objects, as shown in Fig. 3, implying that only longitudinal flow is considered and that the correlative physical quantities are constant in the direction of the fracture aperture. The mass balance equation for gas transport in hydraulic fractures can be written in local coordinates as (Watanabe et al., 2012)

$$\frac{\partial}{\partial t}(c_F w) = -\frac{\partial}{\partial l}(c_F \mathbf{v}_F w) + q_{sF} - q_{fF} \tag{9}$$

where w is the fracture aperture, c_F is the concentration of gas in the hydraulic fracture, l is the dimension along the fracture, $\mathbf{v}_F$ is the average velocity in the fracture, q_{sF} is the sink-source term, and q_{fF} is the leakage flux from the fracture surface to the surrounding natural fracture network.

Due to their high aspect ratio, whereby fracture length is much larger than the aperture, discrete fractures can be idealised as lower dimensional objects. This implies that each physical field is uniform across the fracture width. Fracture flow is considered as a uniform parallel plate, so that $\mathbf{v}_f$ can be described by the well-known cubic law function of the fracture aperture and fluid viscosity (Pouya, 2015; Watanabe et al., 2012), giving

$$\mathbf{v}_F = -\frac{w^2}{12\mu_g}\nabla u_F \tag{10}$$

where $u_F = Z_F RTc_F$ is the gas pressure in the hydraulic fracture and Z_F is the compressibility factor of fluid in the fracture.

Substituting equation (10) into equation (9) and expanding the term on the left-hand side gives

$$w\frac{\partial c_F}{\partial t} + c_F\frac{\partial w}{\partial t} = \frac{\partial}{\partial l}\left(\frac{w^3}{12\mu_g}c_F Z_F RT\frac{\partial c_F}{\partial l}\right) + q_{sF} - q_{fF} \tag{11}$$

It can be seen that the second term on the left-hand side of equation (11) shows an explicit full coupling between fracture flow and the deformation field. The fracture aperture has an impact not only on the hydraulic conductivity but also on the volumetric change of space, the latter usually being omitted in models in the literature (e.g. Moradi et al., 2017; Chen et al, 2019b). When the variation of fracture aperture is not negligible, the flow equation is nonlinear (Watanabe et al., 2012). The change of aperture is described in the following section.

2.4 Coal deformation

2.4.1 Mechanical behaviour of the fracture and matrix continua

The deformation of fractured porous media with a slow-moving fluid is considered as a quasi-static stress equilibrium problem. Different from the mechanical model presented previously (Chen et al., 2019a), the influence of adsorption-induced swelling on coal deformation is represented by modifying the strain field in this work. Considering local stress equilibrium, the changes in total stress within the overlapping continua are identical and the relationship between changes in total stress and the effective stress can be written in incremental form as (Lewis and Pao, 2002; Pao and Lewis, 2002)

$$d\boldsymbol{\sigma}^{\boldsymbol{e}} = d\boldsymbol{\sigma} + \alpha\mathbf{I}du_f + \beta\mathbf{I}du_m \tag{12}$$

where $\boldsymbol{\sigma}$ is the total stress tensor, $\boldsymbol{\sigma}^{\boldsymbol{e}}$ is the effective stress tensor, $\alpha = 1 - \frac{K}{K_m}$ and $\beta = \frac{K}{K_m} - \frac{K}{K_s}$ are Biot coefficients of the fracture and matrix, where $K = E/3(1-2v)$ is the bulk modulus with E being Young's modulus and v being Possion's ratio. $K_m = E_m/3(1-2v)$ is the modulus of the coal matrix with E_m being the coal matrix Young's modulus, which can be obtained from samples an order of magnitude larger than the spacing of the matrix pores but devoid of fractures. K_s is the modulus of the solid constituent and usually cannot be measured directly, however, it can be determined through matching experimental measurements.

The linear elastic stress-strain relationship is defined as

$$d\boldsymbol{\sigma}^{\boldsymbol{e}} = \boldsymbol{D}_e\boldsymbol{\varepsilon}_e \tag{13}$$

where $\boldsymbol{D}_e$ is the elastic stiffness tensor evaluated from lumping deformations in both the matrix and fractures.

The deformation of coal exposed to CO_2 is generally divided into elastic deformation and sorption-induced swelling. The total strain can be given in incremental form as

$$d\boldsymbol{\varepsilon} = d\boldsymbol{\varepsilon}_e + \frac{1}{3}\mathbf{I}d\varepsilon_s \tag{14}$$

where $d\boldsymbol{\varepsilon}$ is the total strain vector, $d\boldsymbol{\varepsilon}_e$is the elastic strain vector, ε_s is the adsorption-induced swelling strain, $\mathbf{I}$ is a vector, and $\mathbf{I}^{\boldsymbol{T}} = (1,1,1,0,0,0)$ and $(1,1,0)$ in three- and two-dimensions, respectively.

Coal swelling can occur locally or globally at different stages of CO_2 injection. Swelling is localised within the vicinity of the fracture compartment at the initial stage of gas injection, which is known as local swelling. As the injection continues, gas diffuses into the coal matrix far from the fracture and the swelling zone extends further into the matrix, with the swelling ultimately switching from local to global. According to Liu et al. (2011) and Qu et al. (2014), the combined influence of both local and global adsorption-induced swelling may be represented using a typical Langmuir-type equation, which is the approach taken in this work, giving

$$\varepsilon_s = \frac{\varepsilon_L u_m}{u_m + u_L} \tag{15}$$

where ε_L is the Langmuir volumetric strain constant.

The strain is related to displacement, expressed as

$$d\boldsymbol{\varepsilon} = \mathbf{P}d\mathbf{u} \tag{16}$$

where $\mathbf{P}$ is the strain-displacement matrix and $\boldsymbol{d}\mathbf{u}$ is a vector of the incremental displacement. The stress equilibrium equation without considering body forces is given as

$$\mathbf{P}^{\boldsymbol{T}} d\boldsymbol{\sigma} + \boldsymbol{F} = 0 \tag{17}$$

where $\boldsymbol{F}$ is the body force vector**.**

2.4.2 Mechanical behaviour of the hydraulic fracture

Natural fractures are represented by the fracture continuum and the deformation of natural fractures is assumed to be continuous and lumped with that of the coal matrix in equation (13). The role of deformation of the fracture continuum is represented by the elastic parameter. The displacement field through the fracture surfaces is discontinuous because of intrinsic mechanical properties of the domain occupied by the hydraulic fractures. The deformation of hydraulic fractures therefore needs to be accounted for explicitly in this section. Following the

work of Watanabe et al. (2012), a discrete fracture is treated as a pair of parallel surfaces between which normal and shear displacements can occur, as shown in Fig. 4. Local fracture relative displacement, defined as the displacement difference between two surfaces of a fracture, is introduced to describe displacement discontinuity along the fracture. Local relative displacements in a local coordinate system (x′, y′) (Fig. 4) are described as

$$\mathbf{w} = \begin{Bmatrix} w_t \\ w_n \end{Bmatrix} = \begin{Bmatrix} u_t^+ - u_t^- \\ u_n^+ - u_n^- \end{Bmatrix} \tag{18}$$

where $\mathbf{w}$ is the local relative displacement vector, the subscripts t and n denote the tangential and normal directions to the fracture plane, respectively, u_t and u_n are the tangential and normal displacements in the local coordinate system, and the superscripts + and – represent the two surfaces of a fracture. Local relative displacements can also be described in terms of global relative displacements in the global coordinate system. Toward this end, the transformation relation between the two coordinate systems is defined as (Fig. 4)

$$\begin{pmatrix} x' \\ y' \end{pmatrix} = \begin{bmatrix} \cos\theta & \sin\theta \\ -\sin\theta & \cos\theta \end{bmatrix} \begin{pmatrix} x \\ y \end{pmatrix} \tag{19}$$

where θ is the angle between the positive x-axis in the global coordinate system and the x'-axis in the local coordinate system.

The local relative displacement is written in terms of the corresponding global relative displacement as

$$\mathbf{w} = \mathbf{R}[\![\mathbf{u}]\!] \tag{20}$$

$$\mathbf{R} = \begin{bmatrix} \cos\theta & \sin\theta \\ -\sin\theta & \cos\theta \end{bmatrix} \tag{21}$$

where $[\![\mathbf{u}]\!]$ is defined as the global relative displacement vector across the two faces of the discontinuity. The symbol $[\![\,]\!]$ denotes the jump across the discontinuity.

In the fractures, the relationship between incremental stress, including mechanical stress and fluid pressure, and the local relative displacement is given as (Deb and Das, 2010; Watanabe et al., 2012)

$$\mathrm{d}\boldsymbol{\sigma}_F' = \boldsymbol{T}\mathrm{d}\mathbf{w} \tag{22}$$

$$\boldsymbol{T} = \begin{bmatrix} k_{tt} & k_{tn} \\ k_{nt} & k_{nn} \end{bmatrix} \tag{23}$$

$$\boldsymbol{\sigma}_F' = \boldsymbol{\sigma}_F + \mathbf{m}^{\mathrm{f}} u_F \tag{24}$$

where $\boldsymbol{\sigma}_F'$ is the effective stress for the fracture, $\boldsymbol{\sigma}_F$ is the total stress vector applied on the fracture plane, u_F is the liquid pressure in the fracture, and $\mathbf{m}^{\mathrm{f}} = \{0, 1\}^{\boldsymbol{T}}$ is the mapping vector. k_{tt} and k_{nn} are the shear and normal

stiffness, respectively. k_{nt} is the slope of the normal stress-shear displacement curve and k_{tn} is the slope of the shear stress-normal displacement curve. However, here we restrict our discussion to the normal stiffness and shear stiffness and assume that $k_{tn} = k_{nt} = 0$.

The local relative normal displacement at two sides of the fracture could induce a change of fracture aperture, which can be expressed with either $\mathbf{w}$ or $[\![\mathbf{u}]\!]$ as

$$w = \mathbf{m}^{f^T}\mathbf{w} = \mathbf{m}^{f^T}\mathbf{R}[\![\mathbf{u}]\!] \tag{25}$$

2.5 Linking deformation with gas flow

In equations (5) and (8), the porosities of the matrix and fracture continua, n_m and n_f, and the permeability of the fracture continuum, k_f, vary with the stress field. In this section, the relationships between these parameters and variable stress fields are derived.

2.5.1 Matrix continuum porosity

The matrix porosity change is related to the effective volumetric strain, ε_{me}, as (Liu et al., 2011)

$$n_m = n_{m0} + \beta\Delta\varepsilon_{me} \tag{26}$$

where n_{m0} is the initial fracture porosity and n_m is the current matrix porosity.

The effective strain of the matrix block, $\Delta\varepsilon_{me}$, is the resultant of the effective stress and the sorption-induced swelling strain, given as (Zhang et al., 2008)

$$\Delta\varepsilon_{me} = \Delta\varepsilon_v - \Delta\varepsilon_s + \frac{\Delta u_m}{K_s} \tag{27}$$

The first term in equation (27) represents the global strain, which can be obtained from the governing equation of mechanical deformation, the second term represents the sorption-induced strain of the matrix, and the last term demonstrates the compressive strain of coal grains.

2.5.2 Fracture continuum porosity and permeability

As shown in Fig. 1a, coal matrix blocks are intersected by sets of cleats or fractures, i.e. face cleats and butt cleats. Under the isotropic conditions, the fracture continuum porosity is therefore

$$n_f = \frac{(a+b)^3 - a^3}{(a+b)^3} \cong \frac{3b}{a} \tag{28}$$

where a is the spacing of natural fractures and b is the aperture of natural fractures.

Similarly, the permeability can be written as (Pan and Connell, 2012)

$$k_f = \frac{a^3}{96} {n_f}^3 \tag{29}$$

The permeability change with respect to a reference state is expressed as

$$\frac{k_f}{k_{f0}} = \left(\frac{a}{a_0}\right)^3 \left(\frac{n_f}{n_{f0}}\right)^3 \tag{30}$$

where the subscript 0 refers to the conditions at the reference state. Considering the matrix size change is negligible compared to the porosity change, i.e. $a \approx a_0$, equation (30) can be reduced as

$$\frac{k_f}{k_{f0}} = \left(\frac{n_f}{n_{f0}}\right)^3 \tag{31}$$

Combined with equation (28), the fracture continuum porosity change with respect to a reference state is obtained

$$\frac{n_f}{n_{f0}} = \frac{b_0 + \Delta b}{b_0} = 1 + \frac{\Delta b}{b_0} \tag{32}$$

where Δb is the change of cleat aperture and b_0 is the initial cleat aperture.

The cleat aperture closure induced by the total effective stress change can be given as (Liu et al., 2010)

$$\Delta b = (a + b)\frac{\Delta \sigma_{et}}{E} - a\frac{\Delta \sigma_{et}}{E_m} \tag{33}$$

Dividing equation (33) by the fracture aperture b and rearranging gives

$$\frac{\Delta b}{b} = \frac{3}{n_{f0}}\left(1 - \frac{E}{E_m}\right)\frac{\Delta \sigma_{et}}{E} + \frac{\Delta \sigma_{et}}{E} \tag{34}$$

Due to $n_{f0} \ll 1$, the last term of equation (34) can be omitted. Assuming that Poisson's ratio is the same for the bulk and matrix, replacing $1 - E/E_m$ with the Biot coefficient, α, and using the total effective strain change, $\Delta \varepsilon_{et}$, to represent $\Delta \sigma_{et}/E$ yields

$$\frac{n_f}{n_{f0}} = 1 + \frac{3\alpha}{n_{f0}} \Delta \varepsilon_{et} \tag{35}$$

The total effective strain change $\Delta \varepsilon_{et}$ is defined as (Liu et al., 2010)

$$\Delta \varepsilon_{et} = \frac{1}{3}(\Delta \varepsilon_v - \Delta \varepsilon_s) \tag{36}$$

Substitution of equations (35) and (36) into equation (31) allows the fracture permeability to be expressed as

$$\frac{k_f}{k_{f0}} = \left[1 + \frac{\alpha}{n_{f0}}(\Delta\varepsilon_v - \Delta\varepsilon_s)\right]^3 \tag{37}$$

3. Finite element formulation

In this study, a numerical solution for the coupled hydro-mechanical behaviour of a fractured porous system is achieved using the finite element method. This section describes the weak formulation of the equilibrium and flow continuity equations as well as the Galerkin finite element method used for discretisation.

3.1 Weak form

The weak formulation of the stress equilibrium and flow continuity equations can be obtained by integrating the product of the equilibrium and mass transfer equations multiplied by admissible test functions over the domain, satisfying the boundary conditions. The weak form of the continuity equations for flow in the porous matrix and fracture are obtained after multiplying the test shape function and integration by parts, giving the following for the porous matrix continuum

$$\int_\Omega \delta c_m C_{mm} \frac{\partial c_m}{\partial t} d\Omega + \int_\Omega \delta c_m C_{mu} \frac{\partial \mathbf{u}}{\partial t} d\Omega - \int_\Omega \delta c_m K_{mm\_f} c_f \, d\Omega - \int_\Omega \delta c_m K_{mm\_m} c_m = \int_\Omega \delta c_m q_{sm} d\Omega \tag{38}$$

and for the fracture continuum

$$\int_\Omega \delta c_f C_{ff} \frac{\partial c_f}{\partial t} d\Omega + \int_\Omega \delta c_f C_{fm} \frac{\partial c_m}{\partial t} d\Omega + \int_\Omega \delta c_f C_{fu} \frac{\partial \mathbf{u}}{\partial t} d\Omega + \int_\Omega \nabla\delta c_f K_{ff} \nabla c_f \, d\Omega - \int_\Omega \delta c_f K_{ff\_f} c_f \, d\Omega - \int_\Omega \delta c_f K_{ff\_m} c_m \, d\Omega = \int_\Omega \delta c_f q_{sf} d\Omega + \int_{\Gamma_q} \delta c_f \overline{q}_f \, d\Gamma + \int_{\Gamma_F} \delta c_F q_{fF} d\Omega \tag{39}$$

and for the discrete fractures

$$\int_{\Gamma_F} \delta c_F C_{FF} \frac{\partial c_F}{\partial t} d\Gamma + \int_{\Gamma_F} \delta c_F C_{F[\![u]\!]} \frac{\partial [\![\mathbf{u}]\!]}{\partial t} d\Gamma + \int_{\Gamma_F} \frac{\partial \delta c_F^T}{\partial l} K_{FF} \frac{\partial c_F}{\partial l} d\Gamma = \int_{\Gamma_F} \delta c_F q_{sF} d\Gamma - \int_{\Gamma_F} \delta c_F q_{fF} d\Gamma + \delta c_f \overline{q}_F \Big|_{L_1}^{L_2} \tag{40}$$

where δc_m, δc_f and δc_F are the test functions, $\overline{q}_f$ and $\overline{q}_F$ are the gas flux through the boundary surface, Γ_{q} is the flux boundary, L_1 and L_2 denote the endpoints of the line element, and C and K are the lumped coefficients presented in Appendix A.

The virtual work equation with body and traction forces reads

$$\int_{\Omega} \nabla^s \delta\mathbf{u}^{\boldsymbol{T}} : \boldsymbol{\sigma} d\Omega - \int_{\Omega} \delta\mathbf{u}^{\boldsymbol{T}} \cdot \boldsymbol{F}\, d\Omega - \int_{\Gamma_t} \delta\mathbf{u}^{\boldsymbol{T}} \cdot \bar{\mathbf{t}}\, d\Gamma - \int_{\Gamma_F} \left(\delta\mathbf{u}^{+\boldsymbol{T}} \cdot \bar{\mathbf{t}}_{\mathrm{d}}^{+} + \delta\mathbf{u}^{-\boldsymbol{T}} \cdot \bar{\mathbf{t}}_{\mathrm{d}}^{-}\right) d\Gamma = 0 \tag{41}$$

where $\delta\mathbf{u}$ is the test function of displacement $\delta\mathbf{u}$ and $\bar{\mathbf{t}}$ is the external traction forces on the boundary Γ_t.

The stress on the discontinuity plane is assumed to be equal but in opposite direction, which leads to

$$\bar{\mathbf{t}}_F^{+} = -\bar{\mathbf{t}}_F^{-} \tag{42}$$

By substituting equation (42), equation (41) can be rewritten as

$$\int_{\Omega} \nabla^s \delta\mathbf{u}^{\boldsymbol{T}} : \boldsymbol{\sigma} d\Omega - \int_{\Omega} \delta\mathbf{u}^{\boldsymbol{T}} \cdot \boldsymbol{F}\, d\Omega - \int_{\Gamma_t} \delta\mathbf{u}^{\boldsymbol{T}} \cdot \bar{\mathbf{t}}\, d\Gamma + \int_{\Gamma_F} \delta[\![\mathbf{u}]\!]^{\boldsymbol{T}} \cdot \bar{\mathbf{t}}_{\mathrm{d}}^{-}\, d\Gamma = 0 \tag{43}$$

where $\delta[\![\mathbf{u}]\!] = \delta\mathbf{u}^{+} - \delta\mathbf{u}^{-}$ represents the test function jump across the discontinuity, Γ_F. The calculation of $\bar{\mathbf{t}}_F^{-}$ and $\bar{\mathbf{t}}_F^{+}$ is addressed in the next section**.**

3.2 Discretised equations

Since we assume fluid concentrations and temperature are continuous over two distinct flow systems (dual porosity media and discrete fractures), the weak forms of the flow continuity equations can be discretised using the standard Galerkin finite element method. Two-node, one-dimensional interface elements are employed for discrete fractures. The fluid concentrations in the dual porosity medium and discrete fractures are approximated as the linear combinations of the standard shape functions as

$$c_m(\mathbf{x}, \mathrm{t}) = \sum_{I_o \in \mathcal{N}_o} N_{I_o}(\mathbf{x}) \hat{c}_{mI_o}(t) \tag{44a}$$

$$c_f(\mathbf{x}, \mathrm{t}) = \sum_{I_o \in \mathcal{N}_o} N_{I_o}(\mathbf{x}) \hat{c}_{fI_o}(t) \tag{44b}$$

$$c_F(\mathbf{x}, \mathrm{t}) = \sum_{I_F \in \mathcal{N}_F} N_{I_F}(\mathbf{x}) \hat{c}_{FI_F}(t) \tag{44c}$$

where N_{I_o} and N_{I_F} are the standard finite element shape functions of nodes I_o and I_F for the discretised overlapping continua and hydraulic fracture domains, respectively. $\mathcal{N}_o$ and $\mathcal{N}_F$ are the set of all nodes in the discretised overlapping continua and hydraulic fracture domains, respectively, and the symbol $\widehat{\ }$ denotes the approximate value of the primary variable.

Due to the presence of discrete fractures, the displacement function **u**(x) is strongly discontinuous at the discontinuity plane, Γ_F, making it difficult to solve the discontinuous problem using continuity based numerical methods such as the finite element method. Lower-dimensional interface elements with local enrichment approximations were proposed by Watanabe et al. (2012) to approximate the discontinuous displacement function and the global fracture relative displacement functions. The approximation of the displacement function is expressed as

$$\mathbf{u}(\mathbf{x},\mathrm{t}) = \sum_{I_o \in \mathcal{N}_o} N_{I_o}(\mathbf{x})\hat{\mathbf{u}}_{I_o}(t) + \sum_{I_o \in I_F} N_{I_o}(\mathbf{x})\psi_F(\mathbf{x})\boldsymbol{a}_{I_o}(t) \tag{45}$$

where $\hat{\mathbf{u}}_i$ are the standard displacement degrees of freedom at nodes I_u, corresponding to the standard finite element approximation, and $\boldsymbol{a}_i$ is the displacement jump function at enriched nodes I_F on the discontinuity Γ_F, corresponding to the local enrichment approximation. ψ_d is a global enrichment function, which can be described with the Heaviside step function as

$$\psi_F(\mathbf{x}) = H\big(f_F(\mathbf{x})\big) = \begin{cases} 1 & \text{for } \mathrm{x} \in \Omega_+ \\ 0 & \text{for } \mathrm{x} \in \Omega_- \end{cases} \tag{46}$$

in which $f_F(\mathbf{x})$ is a signed distance function, giving positive if x is in a region $\Omega^+$and negative in Ω^-.

For a single discontinuity, the jump function is identical to the global fracture relative displacement

$$[\![\mathbf{u}]\!] = \boldsymbol{a} \tag{47}$$

And the finite element approximation of the global relative displacement function $[\![\mathbf{u}]\!]$ is given as

$$[\![\mathbf{u}]\!] = \sum_{I_o \in I_d} N_{I_o}(\mathbf{x})a_{I_o}(t) = \boldsymbol{N}_{\mathrm{u}}^F\boldsymbol{a} \tag{48}$$

To reduce the dimension of fractures, we assume the fluid concentration and temperature should be continuous at the matrix–fracture interface, that is $\hat{c}_{FI_F} = \hat{c}_{fI_o}$, and the one-dimensional interface element is used for fracture representation sharing nodes with the elements of the porous medium, as shown in Fig. 5. Coupling between the

two flow systems is achieved through superposition. The mass exchange term between the hydraulic fracture and natural fracture networks in equations (6) and (9), q_{fF}, balances off and no explicit calculation is required.

Substitution of the approximate values of the primary variables in equations (47), (48) and (51) into the weak formulations (41)-(43) and (46), with integration by parts after multiplying the test shape functions, results in the discretised form of governing equations, as

$$\begin{bmatrix} \boldsymbol{C}_{mm} & \mathbf{0} & \boldsymbol{C}_{m\mathrm{u}} & \mathbf{0} \\ \boldsymbol{C}_{fm} & \boldsymbol{C}_{ff}+\boldsymbol{C}_{FF} & \boldsymbol{C}_{f\mathrm{u}} & \boldsymbol{C}_{F\mathrm{a}} \\ \boldsymbol{C}_{\mathrm{u}m} & \boldsymbol{C}_{\mathrm{u}f} & \boldsymbol{C}_{\mathrm{uu}} & \boldsymbol{C}_{\mathrm{u}a} \\ \mathbf{0} & \boldsymbol{C}_{af} & \boldsymbol{C}_{a\mathrm{u}} & \boldsymbol{C}_{aa} \end{bmatrix} \begin{bmatrix} \dot{\hat{\mathbf{c}}}_m \\ \dot{\hat{\mathbf{c}}}_f \\ \dot{\mathbf{u}} \\ \dot{\mathbf{a}} \end{bmatrix} + \begin{bmatrix} \boldsymbol{K}_{mm\_m} & \boldsymbol{K}_{mm\_f} & \mathbf{0} & \mathbf{0} \\ \boldsymbol{K}_{ff\_m} & \boldsymbol{K}_{ff}+\boldsymbol{K}_{FF}+\boldsymbol{K}_{ff\_f} & \mathbf{0} & \mathbf{0} \\ \mathbf{0} & \mathbf{0} & \mathbf{0} & \mathbf{0} \\ \mathbf{0} & \mathbf{0} & \mathbf{0} & \mathbf{0} \end{bmatrix} \begin{bmatrix} \hat{\mathbf{c}}_m \\ \hat{\mathbf{c}}_f \\ \mathbf{u} \\ \boldsymbol{a} \end{bmatrix} = \begin{bmatrix} \mathbf{f}_{c_m} \\ \mathbf{f}_{c_f} \\ \mathbf{f}_{\mathrm{u}} \\ \mathbf{f}_{\mathrm{a}} \end{bmatrix} \tag{49}$$

These matrices are constructed according to Appendix B.

The numerical formulation has been incorporated into the numerical code, COMPASS. For temporal discretisation, an implicit mid-interval forward difference time-stepping algorithm is employed.

4. Model verification and validation

Two verification tests are presented using known analytical solutions as benchmarks. The first test looks at the enrichment finite element approximation by considering a single fracture under static stress. The reliability of the developed model in coupled HM analysis is addressed by the second verification test by examining Wijesinghe's problem, which has been widely used to test coupled fracture codes (Noorishad et al., 1992; Watanabe et al., 2012). After that, the model's ability to predict gas flow and interactions in coal is examined, which is achieved by comparing numerical results with experimental data by Pini et al. (2009).

4.1 Single fracture under static stress

This verification test considers the pure elastic response of a central discontinuity within a 2D linear, homogenous and isotropic rock, as shown in Fig. 6a. A constant stress is applied on the top of the rock and a plane strain condition is assumed. The applied stress is $\sigma_T = 5$ MPa, and Young's modulus and Poisson's ratio are $E = 25$ GPa and $v = 0.25$, respectively. The fracture length is defined as $2\mathrm{L} = 20$ m. The analytical solution of this purely mechanical problem is available in Garipov et al. (2016). The fracture aperture is given as

$$\Delta a(x) = \frac{4L\sigma_{\mathrm{T}}(1-v^2)}{E}\sqrt{1-\frac{x^2}{L^2}} \tag{50}$$

Fig. 6b compares the numerical and analytical solutions for the fracture opening. There is a good agreement between the two sets of results, which provides confidence in the accuracy of the enrichment finite element method used in this work.

4.2 Wijesinghe's problem

This test considers coupled one dimensional transient fluid flow and stress in a single discrete fracture with variable aperture surrounded by an impermeable rock matrix, as shown in Fig. 7. Wijesinghe (1986) derived a semi-analytical solution using the cubic law to model fracture permeability and constant fracture stiffness. This same problem is solved here using COMPASS. The fracture is 25 m long with a normal stiffness of 1.0×10^{11} N/m. Flow of a single incompressible gas component is considered with a dynamic viscosity of 1.84 Pa s. Initially, the fracture aperture is uniformly 1.0×10^{-5} m with a fluid pressure of 1 MPa along the fracture. At time $t = 0$, gas is injected into the fracture at a pressure of 1.9 MPa. The fracture aperture is forced to increase as the pressure front moves along the fracture.

A comparison of the results of COMPASS with Wijesinghe's semi-analytical solution at 500 s and 2000 s is presented in Fig. 8. The openings are a linear function of gas pressure. When the fluid is injected, the fracture opening is instantaneously increased to 1.9×10^{-5} m at the injection position. With the movement of the pressure front, the fracture opening gradually propagates down the fracture. Fig. 8 shows that an agreement between the numerical and analytical solutions is achieved.

4.3 Comparison with experimental data

Pini et al. (2009) performed flow experiments on coal cores under hydrostatic confinement. A bituminous coal sample 2.54 cm in diameter and 3.6 cm in length was obtained using coal from the Monte Sinni mine in the Sulcis Coal Province (Sardinia, Italy). The transient method was adopted and CO_2 and N_2 were used to investigate the effects of adsorption and swelling on the flow dynamics under constant and varying confining pressure. In this validation test, the experimental results for CO_2 injection are used to examine the performance of the developed model in terms of describing the flow and deformation characteristics involved. The effects of hydraulic fractures are neglected due to the absence of any such fractures in the coal core.

A cylindrical geometry (3.6 cm in length and 2.54 cm in diameter) confined by a constant stress of 10 MPa is selected for the numerical simulation, as shown in Fig. 9a. Due to the symmetry, the cylindrical coal sample can be simplified as the 2D model shown in Fig. 9b. Boundary conditions corresponding to the conditions shown in

Fig. 9b are applied. For coal deformation, a vertical constraint is applied to the inflow and outflow boundaries while a constant confining stress is applied to the right-hand boundary. The left side of the model is fixed horizontally. For gas flow, a zero-flux boundary is applied to the right and left boundaries. A time dependent upstream pressure is used as the injection boundary condition. The initial pressure for both the fracture and matrix continua is 1.0 MPa. The material parameters used in this test are from Pini et al. (2009), Guo et al. (2014), and Zang and Wang (2016), as listed in Table 1.

Fig. 10 shows the comparison of transient steps performed with CO_2 under constant confining pressure; symbols denote the experimental measurements whereas lines show the model results. There is a good agreement between experimental measurements and numerical predictions, indicating that the proposed model can describe the coupled behaviour of coal during CO_2 injection under the conditions considered.

5. Numerical simulation and discussion

5.1 Model description

A model problem of CO_2 injection into a coal seam is considered to study the influence on the stress field and permeability. The simulation domain considered is shown in Fig. 11. It is a 2D plane square (x-y) domain with a length of 300 m and a 0.1 m radius injection well located at the bottom-left corner of the model. There is a hydraulic fracture connecting to the injection well, which has a length of 30 m with a width of 2 mm. Coal seams are often horizontal or sub-horizontal and confined by much stronger and thicker formations at their top and base. The horizontal deformation or strain is predominant within coal seams and vertical deformation is negligible due to the very small vertical-horizontal ratio of the coal seam. Therefore, the simulations are conducted under plane strain conditions (e.g. Cui et al. 2007; Saliya et al. 2015). The simulations are hypothetical but retain physical relevance since the property values are taken from studies on the Ishikari Coal Basin of Japan (Fujioka et al., 2010; Yamaguchi et al., 2005). The purpose of this simulation is to study the effect of a hydraulic fracture on the injection of CO_2 into a coal seam. The mechanical behaviour of the fracture is not the principal focus and so it is assumed that it does not further propagate and has constant mechanical properties.

Table 2 lists the material parameters used. The well operational conditions used during the simulation comprise an initial period of primary production before CO_2 injection, leading to a residual reservoir pressure of 0.7 MPa after the extraction of water and coalbed methane. In the simulation, this pressure is assumed to be induced by a small quantity of the CO_2 injected. The coal seam is located at a depth of 930 m with an average overburden

density of 2500 kg/m^3, giving the assumed vertical boundary loading of 23 MPa. The displacements at the left and bottom sides are constrained in the horizontal and vertical directions. An isotropic horizontal stress of 12.5 MPa is applied to the top and right sides. For fluid flow, a zero-flux boundary is used on all boundaries except on the boundary of the well. The finite element domain is discretised using 4-noded isoparametric quadrilateral elements with varying mesh size, as shown in Fig. 11b. The model is run for two cases, with and without a hydraulic fracture, in which CO_2 is continuously injected into the coal seam at a constant injection pressure of 8 MPa in excess of the initial pressure.

5.2 Numerical results and discussion

Fig. 12 shows the distribution of gas pressure in the fracture continuum at 10 days, 30 days, and 90 days for the simulations with and without the hydraulic fracture. The injected gas flows radially outward from the wellbore into the coal seam when the hydraulic fracture is absent, which produces a uniform pressure distribution around the wellbore, as shown in Fig. 12a. For the simulation with the hydraulic fracture, the gas prefers to flow within the hydraulic fracture due to its higher permeability, thereby penetrating the domain surrounding the fracture. The gas pressure in the hydraulic fracture is almost identical to the injection pressure and so its presence both influences the distribution of gas pressure and improves the gas flow rate. As expected, the CO_2 advances more rapidly into the coal seam. This is because the hydraulic fracture forms a larger area of elevated fluid pressure, resulting in a higher flow rate into the coal seam. The higher gas pressure in the fracture continuum accelerates the penetration of gas into the coal matrix; hence, gas pressure in the matrix continuum displays a similar distribution and the contour plots of matrix pressure distribution are not shown.

The evolution of pore pressure at coordinate locations (expressed in meters) in the vicinity of the wellbore are shown in Fig. 13. These points are located at horizontal distances of 1 m, 3 m and 10 m from the wellbore. Both simulation cases show that gas pressure in the fracture continuum is quicker to reach steady state than in the matrix continuum at the three monitored points. Gas pressure in the matrix continuum at locations further from the wellbore catches up to the pressure in the fracture continuum before reaching the steady state. The further the location is away from the wellbore, the lower this pressure is, especially for the simulation with no hydraulic fracture, as shown in Fig. 13a. The time for gas pressure in the matrix continuum to reach the pressure of the fracture continuum is different in the scenarios with and without the hydraulic fracture. With the hydraulic fracture, the time for the matrix gas pressure to reach the fracture pressure is shorter, as shown in Fig. 13b. In other words, the presence of the hydraulic fracture reduces the equilibrium time of the matrix pressure. This can be explained

by the fact that an area with higher gas pressure is formed around the hydraulic fracture, within which the mass exchange rate is increased due to the higher pressure (i.e. concentration) difference between the matrix and fracture continua.

Coupled to the gas flow, CO_2 injection disturbs the in-situ stress field of the coal seam. Accordingly, the changes in stress state at horizontal distances of 1 m, 3 m and 10 m from the injection well for the two simulation scenarios are shown in Fig. 14. The evolution of stress in both simulation scenarios shows a similar trend. Overall, both horizontal stress and vertical stress increase at first, as observed in field tests, and then decrease gradually after reaching a maximum value. There is a slight decrease in both horizontal stress (σ_{xx}, σ_{yy}) and vertical stress (σ_{zz}) at all locations in the simulation scenario with the hydraulic fracture and at the far field of the simulation case without a hydraulic fracture in the early stages, as show in Fig. 14c-f. Compared with the change in horizontal stress, CO_2 injection leads to a larger increase in vertical stress for both simulations, which implies the effect of adsorption-induced swelling on vertical stress is stronger than on the horizontal stress. Furthermore, the increase of stress is postponed and the starting time for this reduction is earlier at locations further from the wellbore, especially for the simulation without the hydraulic fracture. It can be seen that the presence of the hydraulic fracture has a negligible effect on the maximum stress induced by coal swelling, however, it can make the reduction in stress start earlier and produces a larger decline in both horizontal and vertical stress; the horizontal stress at the later stage is even lower than the initial stress, as shown in Fig.14d-f. It is worth noting that CO_2 injection has a negligible effect on the change in tangential stress (σ_{xy}), as shown in Fig. 15.

Fig. 16 shows the variation of fracture continuum permeability with time at horizontal distances of 1 m, 3 m and 10 m from the injection well for the two simulation scenarios. By comparing the changes in permeability and the stress field, permeability varies in a consistent manner with stress, as expected because it is controlled by the stress field. For the simulation without the hydraulic fracture, the permeability near the injection well decreases, in contrast to the permeability variation in the far-field, which shows a slight increase driven by the increase of fracture pressure. Because the pressure difference between the two continua near the injection well is larger, more gas penetrates the coal matrix and causes swelling, thereby restraining the effect of the elevated fracture pressure. After decreasing to a minimum, permeability starts to recover as injection continues, as shown in Fig. 16a. Even though the permeability in the simulation with the hydraulic fracture displays a similar pattern, the differences between the two simulation cases are worth noting. Due to the higher permeability of the hydraulic fracture, the time taken for permeability to reach the minimum is reduced, which in turn leads to the permeability recovery

starting earlier compared to when the hydraulic fracture is not present. Therefore, the permeability increase in the simulation with the hydraulic fracture is larger.

Fig. 17 presents a comparison of the cumulative amount of CO_2 injected to illustrate the influence of the hydraulic fracture. The presence of the hydraulic fracture results in a significant increase in the CO_2 injectivity; the cumulative injection with the hydraulic fracture is double that without the hydraulic fracture. The hydraulic fracture provides a preferential flow pathway for CO_2 transport and produces a large contact area with a higher fluid pressure within the coal seam, meaning that more CO_2 penetrates the coal matrix and becomes adsorbed.

The new capability of the numerical model to simulate the behaviour described above is highly significant for the study of CO_2 sequestration in coal seams, since hydraulic fracture stimulation has been successfully applied in several field experiments (Fujioka et al., 2010; van Bergen et al., 2009).

6. Conclusions

Among the options for CO_2 capture, utilisation and sequestration, the potential for sequestration in coal is presently restricted by its naturally low permeability and the injectivity loss caused by CO_2 adsorption-induced coal swelling. Hydraulic fracturing is considered a feasible way to improve CO_2 injectivity, however the coupled flow and geomechanical effects on CO_2 sequestration are not clear. This work has presented a hybrid model of coupled compressible fluid flow, adsorption and geomechanics to investigate the impacts of hydraulic fractures on the stress field of coal and CO_2 injectivity. The natural fracture network and porous coal matrix have been described using a dual porosity model with the hydraulic fractures represented explicitly using lower-dimensional interface elements. The coupling between the two different models has been achieved using the principle of superposition for fluid continuity and the local enrichment approximation for displacement discontinuity at the surface of a hydraulic fracture. The Galerkin finite element method has been used to numerically solve the governing equations with verification provided by comparing numerical results with known analytical solutions. An application of the model has been presented to study the effects of a hydraulic fracture on the flow behaviour and stress field within a coal seam during CO_2 sequestration.

Simulation results show that the presence of a hydraulic fracture influences the distribution of gas pressure and improves the gas flow rate, as expected. CO_2 injection disturbs the stress field of a coal seam, causing an increase in horizontal and vertical stresses, especially the latter. Compared to the variation of stress with no hydraulic fracture, the reduction in stress with a hydraulic fracture starts earlier, which causes a larger decline in both horizontal and vertical stress after reaching a maximum value. Permeability is controlled by the stress; hence, the

time taken for permeability to reach a minimum is reduced when the hydraulic fracture is present and permeability recovery starts earlier, thereby showing a larger increase during the same period. The work presented in this paper provides important insights into the behaviour governing CO_2 flow and stress field changes in the presence of a hydraulic fracture, which is particularly relevant considering the current reliance of the technology on this technique based on the majority of field trials.

Acknowledgments

The financial support provided by the China Scholarship Council for the PhD studentship of the first author is gratefully acknowledged. The financial support provided by the Welsh European Funding Office (WEFO), through the FLEXIS project, is also gratefully acknowledged.

Appendix A

The coefficients of the governing equations are

$$C_{mm} = n_m + \frac{\partial c_s}{\partial c_m} + \frac{\beta}{K_s} Z_m RT c_m - c_m \beta \frac{\partial \varepsilon_s}{\partial c_m}$$

$$C_{mu} = c_m \beta \mathbf{I}^{\boldsymbol{T}} \boldsymbol{P}$$

$$K_{mm\_f} = \frac{1}{\tau}$$

$$K_{mm\_m} = -\frac{1}{\tau}$$

$$C_{ff} = n_f$$

$$C_{fm} = -c_f \alpha \frac{\partial \varepsilon_s}{\partial c_m}$$

$$C_{fu} = c_f \alpha \mathbf{I}^{\boldsymbol{T}} \boldsymbol{P}$$

$$K_{ff} = \frac{k_f}{\mu} Z_f RT c_f$$

$$K_{ff\_f} = -\frac{1}{\tau}$$

$$K_{ff\_m} = \frac{1}{\tau}$$

$$C_{FF} = w$$

$$C_{F[\![u]\!]} = c_F \mathbf{m}^{\mathbf{f^T}} \mathbf{R}$$

$$K_{FF} = \frac{w^3}{12\mu_g} c_F Z_F RT$$

$$C_{uf} = \boldsymbol{P}\mathbf{I}\alpha Z_f RT$$

$$C_{um} = \boldsymbol{P}\mathbf{I}\left[\frac{1}{3}\frac{\partial \varepsilon_s}{\partial c_m} + \beta Z_m RT\right]$$

$$C_{uu} = \boldsymbol{P}\mathbf{D}\boldsymbol{P}^{\boldsymbol{T}}$$

where $\boldsymbol{P}$ represents the strain matrix.

Appendix B

The elements of the listed matrices are

$$\boldsymbol{C}_{mm} = \int_{\Omega} \boldsymbol{N}_o^T C_{mm} \boldsymbol{N}_o \, d\Omega$$

$$\boldsymbol{C}_{mu} = \int_{\Omega} \boldsymbol{N}_o^T C_{mu} \boldsymbol{N}_o \, d\Omega$$

$$\boldsymbol{K}_{mm\_m} = \int_{\Omega} \boldsymbol{N}_o^T K_{mm\_m} \boldsymbol{N}_o \, d\Omega$$

$$\boldsymbol{K}_{mm\_f} = \int_{\Omega} \boldsymbol{N}_o^T K_{mm\_f} \boldsymbol{N}_o \, d\Omega$$

$$\boldsymbol{C}_{fm} = \int_{\Omega} \boldsymbol{N}_o^T C_{fm} \boldsymbol{N}_o \, d\Omega$$

$$\boldsymbol{C}_{ff} = \int_{\Omega} \boldsymbol{N}_o^T C_{ff} \boldsymbol{N}_o \, d\Omega$$

$$\boldsymbol{C}_{FF} = \int_{\Gamma_d} \boldsymbol{N}_F^T C_{FF} \boldsymbol{N}_F d\Gamma$$

$$\boldsymbol{C}_{f\mathrm{u}} = \int_{\Omega} \boldsymbol{N}_o^T C_{fu} \boldsymbol{N}_o \, d\Omega$$

$$\boldsymbol{C}_{F\mathrm{a}} = \int_{\Gamma_d} \boldsymbol{N}_F^T \boldsymbol{R}^T Z_f RT \mathbf{m}^{\mathrm{f}} \boldsymbol{N}_F d\Gamma_d$$

$$\boldsymbol{K}_{ff\_m} = \int_{\Omega} \boldsymbol{N}_o^T K_{ff\_m} \boldsymbol{N}_o \, d\Omega$$

$$\boldsymbol{K}_{ff} = \int_{\Omega} \nabla \boldsymbol{N}_o^T K_{ff} \nabla \boldsymbol{N}_o \, d\Omega$$

$$\boldsymbol{K}_{ff\_f} = \int_{\Omega} \boldsymbol{N}_o^T K_{ff\_f} \boldsymbol{N}_o \, d\Omega$$

$$\boldsymbol{K}_{FF} = \int_{\Gamma_d} \boldsymbol{N}_F^T K_{FF} \boldsymbol{N}_F d\Gamma$$

$$\boldsymbol{C}_{\mathrm{um}} = \int_{\Omega} \boldsymbol{B} \left[\left(\varphi_f b_f + \varphi_m b_m - \varphi_f \right) \frac{B Z_m R^2 T^2}{1 + B u_m} + b_m Z_m RT \right] \mathbf{I} \boldsymbol{N}_o d\Omega_m$$

$$\boldsymbol{C}_{\mathrm{u}f} = \int_{\Omega} \boldsymbol{B} b_f Z_f RT \boldsymbol{N}_o \, d\Omega$$

$$\boldsymbol{C}_{\mathrm{uu}} = \int_{\Omega} \boldsymbol{B} D_e \boldsymbol{B}^T \, d\Omega$$

$$\boldsymbol{C}_{\mathrm{u}a} = \int_{\Omega^+} \psi_d \, \boldsymbol{B} D_e \boldsymbol{B}^T \, d\Omega$$

$$\boldsymbol{C}_{af} = \int_{\Gamma_d} \boldsymbol{N}_f^T \boldsymbol{R}^T Z_f RT \mathbf{m}^{\mathrm{f}} \boldsymbol{N}_f d\Gamma_d$$

$$\boldsymbol{C}_{a\mathrm{u}} = \int_{\Omega^+} \psi_d \, \boldsymbol{B}^T D_e \, \boldsymbol{B} d\Omega$$

$$\boldsymbol{C}_{aa} = \int_{\Omega^+} \psi_d \boldsymbol{B} D_e \boldsymbol{B}^T \, d\Omega + \int_{\Gamma_d} \boldsymbol{N}_{\mathrm{u}}^F \boldsymbol{R}^T \boldsymbol{T} \boldsymbol{R} \boldsymbol{N}_{\mathrm{u}}^F d\Gamma_d$$

$$\mathbf{f}_{c_m} = \int_{\Omega} \boldsymbol{N}_o^T q_{sm} \, d\Omega$$

$$\mathbf{f}_{c_f} = \int_{\Omega} \delta c_f q_{sf} d\Omega + \int_{\Gamma_{\mathrm{q}}} \boldsymbol{N}_o^T \overline{q}_f \, d\Gamma + \int_{\Gamma_F} \delta c_F q_{sF} d\Gamma + \delta c_f \overline{q}_F \Big|_{L_1}^{L_2}$$

$$\mathbf{f}_{\mathrm{u}} = \int_{\Omega} \boldsymbol{N}_o^T \boldsymbol{F} d\Omega + \int_{\Gamma_{\mathrm{t}}} \boldsymbol{N}_o^T \overline{t} \, d\Gamma_{\mathrm{t}}$$

$$\mathbf{f}_{\mathrm{a}} = \int_{\Gamma_d} \psi_F \boldsymbol{N}_{\mathrm{u}}^{fT} \overline{t} \, d\Gamma_{\mathrm{t}}$$

where $\boldsymbol{B}=\boldsymbol{P}\boldsymbol{N}_o$

References

Biot, M.A., Temple, G., 1972. Theory of finite deformations of porous solids. Indiana University Mathematics Journal 21, 597-620.

Chen, M., Hosking, L.J., Sandford, R.J., Thomas, H.R., 2019. Dual porosity modelling of the coupled mechanical response of coal to gas flow and adsorption. International Journal of Coal Geology.

Cui, X., Bustin, R.M. and Chikatamarla, L., 2007. Adsorption‐induced coal swelling and stress: Implications for methane production and acid gas sequestration into coal seams. Journal of Geophysical Research: Solid Earth, 112(B10).

Deb, D., Das, K.C., 2010. Extended finite element method for the analysis of discontinuities in rock masses. Geotechnical and Geological Engineering 28, 643-659.

Fujioka, M., Yamaguchi, S., Nako, M., 2010. CO_2-ECBM field tests in the Ishikari Coal Basin of Japan. International Journal of Coal Geology 82, 287-298.

Garipov, T., Karimi-Fard, M., Tchelepi, H., 2016. Discrete fracture model for coupled flow and geomechanics. Computational Geosciences 20, 149-160.

Guo, P., Cheng, Y., Jin, K., Li, W., Tu, Q. and Liu, H., 2014. Impact of effective stress and matrix deformation on the coal fracture permeability. Transport in porous media, 103(1), 99-115.

Goodman, R.E., Taylor, R.L., Brekke, T.L., 1968. A model for the mechanics of jointed rock. Journal of Soil Mechanics & Foundations Div.

Hosking, L.J., Thomas, H.R., Sedighi, M., 2017. A dual porosity model of high-pressure gas flow for geoenergy applications. Canadian Geotechnical Journal 55, 839-851.

Jing, L., 2003. A review of techniques, advances and outstanding issues in numerical modelling for rock mechanics and rock engineering. International Journal of Rock Mechanics and Mining Sciences 40, 283-353.

Lewis, R., Pao, W., 2002. Numerical simulation of three-phase flow in deforming fractured reservoirs. Oil & Gas Science and Technology 57, 499-514.

Lisjak, A. and Grasselli, G., 2014. A review of discrete modeling techniques for fracturing processes in discontinuous rock masses. Journal of Rock Mechanics and Geotechnical Engineering, 6(4), pp.301-314.

Liu, J., Chen, Z., Elsworth, D., Miao, X., Mao, X., 2010. Evaluation of stress-controlled coal swelling processes. International journal of coal geology 83, 446-455.

Liu, J., Chen, Z., Elsworth, D., Qu, H., Chen, D., 2011. Interactions of multiple processes during CBM extraction: a critical review. International Journal of Coal Geology 87, 175-189.

Liu, J., Wang, J., Chen, Z., Wang, S., Elsworth, D. and Jiang, Y., 2011. Impact of transition from local swelling to macro swelling on the evolution of coal permeability. International Journal of Coal Geology 88, 31-40.

Mahabadi, O.K., Lisjak, A., Munjiza, A. and Grasselli, G., 2012. Y-Geo: new combined finite-discrete element numerical code for geomechanical applications. International Journal of Geomechanics 12, 676-688.

Masum, S.A., Thomas, H.R., 2018. Modelling coupled microbial processes in the subsurface: Model development, verification, evaluation and application. Advances in Water Resources 116, 1-17.

Mohammadnejad, T., Khoei, A., 2013. Hydro-mechanical modeling of cohesive crack propagation in multiphase porous media using the extended finite element method. International Journal for Numerical and Analytical Methods in Geomechanics 37, 1247-1279.

Moradi, M., Shamloo, A., Dezfuli, A.D., 2017. A sequential implicit discrete fracture model for three-dimensional coupled flow-geomechanics problems in naturally fractured porous media. Journal of Petroleum Science and Engineering 150, 312-322.

Munjiza, A.A., 2004. The combined finite-discrete element method. John Wiley & Sons.

Ng, K., Small, J., 1997. Behavior of joints and interfaces subjected to water pressure. Computers and Geotechnics 20, 71-93.

Noorishad, J., Tsang, C.-F., Witherspoon, P., 1992. Theoretical and field studies of coupled hydromechanical behaviour of fractured rocks—1. Development and verification of a numerical simulator, International Journal of Rock Mechanics and Mining Sciences & Geomechanics Abstracts. Elsevier, 401-409.

Pan, Z., Connell, L.D., 2012. Modelling permeability for coal reservoirs: a review of analytical models and testing data. International Journal of Coal Geology 92, 1-44.

Pan, Z., Ye, J., Zhou, F., Tan, Y., Connell, L.D., Fan, J., 2018. CO_2 storage in coal to enhance coalbed methane recovery: a review of field experiments in China. International Geology Review 60, 754-776.

Pao, W.K., Lewis, R.W., 2002. Three-dimensional finite element simulation of three-phase flow in a deforming fissured reservoir. Computer methods in applied mechanics and engineering 191, 2631-2659.

Peng, D.-Y., Robinson, D.B., 1976. A new two-constant equation of state. Industrial & Engineering Chemistry Fundamentals 15, 59-64.

Peng, Y., Liu, J., Wei, M., Pan, Z., Connell, L.D., 2014. Why coal permeability changes under free swellings: New insights. International Journal of Coal Geology 133, 35-46.

Pini, R., Ottiger, S., Burlini, L., Storti, G. and Mazzotti, M., 2009. Role of adsorption and swelling on the dynamics of gas injection in coal. Journal of Geophysical Research: Solid Earth, 114(B4).

Pouya, A., 2015. A finite element method for modeling coupled flow and deformation in porous fractured media. International Journal for Numerical and Analytical Methods in Geomechanics 39, 1836-1852.

Qu, H., Liu, J., Pan, Z. and Connell, L., 2014. Impact of matrix swelling area propagation on the evolution of coal permeability under coupled multiple processes. Journal of Natural Gas Science and Engineering 18, 451-466

Réthoré, J., Borst, R.d., Abellan, M.A., 2007. A two-scale approach for fluid flow in fractured porous media. International Journal for Numerical Methods in Engineering 71, 780-800.

Salimzadeh, S., Khalili, N., 2015. Fully coupled XFEM model for flow and deformation in fractured porous media with explicit fracture flow. International Journal of Geomechanics 16, 04015091.

Saliya, K., Grgic, D., Giot, R. and Giraud, A., 2015. Thermo-hydro-mechanical modeling with Langmuir's adsorption isotherm of the CO_2 injection in coal. International Journal for Numerical and Analytical Methods in Geomechanics, 39(6), pp.594-617.

Thomas, H.R., He, Y., 1998. Modelling the behaviour of unsaturated soil using an elastoplastic constitutive model. Géotechnique 48, 589-603.

van Bergen, F., Krzystolik, P., van Wageningen, N., Pagnier, H., Jura, B., Skiba, J., Winthaegen, P., Kobiela, Z., 2009. Production of gas from coal seams in the Upper Silesian Coal Basin in Poland in the post-injection period of an ECBM pilot site. International Journal of Coal Geology 77, 175-187.

Watanabe, N., Wang, W., Taron, J., Görke, U., Kolditz, O., 2012. Lower-dimensional interface elements with local enrichment: application to coupled hydro-mechanical problems in discretely fractured porous media. International Journal for Numerical Methods in Engineering 90, 1010-1034.

Wijesinghe, A.M., 1986. A similarity solution for coupled deformation and fluid flow in discrete fractures, 2nd International conference on radioactive waste management, pp. 349.

Yamaguchi, S., Ohga, K., Fujioka, M., Muto, S., 2005. Prospect of CO_2 sequestration in the Ishikari coal field, Japan, Greenhouse Gas Control Technologies 7. Elsevier, 423-430.

Zang, J. and Wang, K., 2016. A numerical model for simulating single-phase gas flow in anisotropic coal. Journal of Natural Gas Science and Engineering, 28, 153-172.

Zhang, H., Liu, J., Elsworth, D., 2008. How sorption-induced matrix deformation affects gas flow in coal seams: a new FE model. International Journal of Rock Mechanics and Mining Sciences 45, 1226-1236.

Tables

Table 1 Parameters used for the validation test.

Parameter	**Value**	**Unit**
Young's modulus of coal, E	1.12	GPa
Biot coefficient, α	0.075	-
Biot coefficient, β	0.925	-
Poisson's ratio, v	0.26	-
Initial permeability, k_{f0}	1.1e-19	m^2
Initial matrix porosity n_{m0}	2	%
Initial fracture porosity n_{f0}	0.42	%
Density of coal, ρ_c	1356.6	kg/m^3
Viscosity of gas, μ_g	1.6e-5	Pa·s
Langmuir volume constant, V_L	2.49	mol/kg
Langmuir pressure, u_L	2.63	MPa
Langmuir volumetric constant, ε_L	4.9	%
Sorption time, τ	2.58e5	s
Formation temperature, T	318.15	K
Gas constant, R	8.314	J/mol/K

Table 2 Material parameters used for the numerical simulations.

Parameter	**Value**	**Unit**
Young's modulus of coal, E	2.92	GPa
Biot coefficient, α	0.27	-
Biot coefficient, β	0.73	-
Poisson's ratio, v	0.35	-
Initial permeability, k_{f0}	1.0	mD
Initial matrix porosity n_{m0}	5.5	%
Initial fracture porosity n_{f0}	1	%
Density of coal, ρ_c	1337	kg/m^3
Viscosity of gas, μ_g	1.84e-5	Pa s
CO_2 Langmuir volume constant, V_L	1.97	mol/kg
CO_2 Langmuir pressure, u_L	0.97	MPa
CO_2 Langmuir volumetric constant, ε_L	1.23	%
Sorption time, τ	2.5	days
Formation temperature, T	303	K
Gas constant, R	8.314	J/mol/K
Normal stiffness, K_n	100	GPa/m
Shear stiffness, K_t	100	GPa /m

Figures

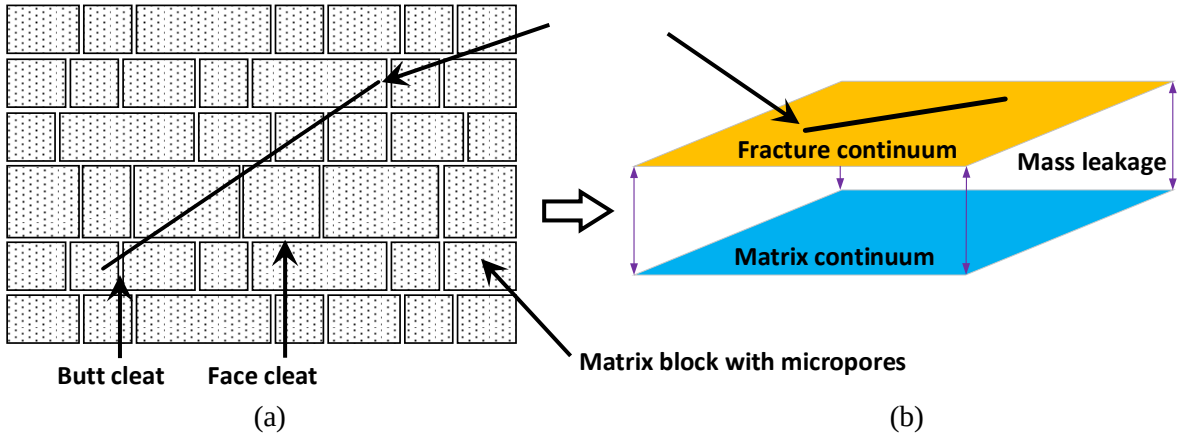

Fig. 1 (a) A schematic of naturally fractured coal in plan view, and (b) a conceptualisation of the hybrid dual porosity model developed in this work, embedded with a single hydraulic fracture.

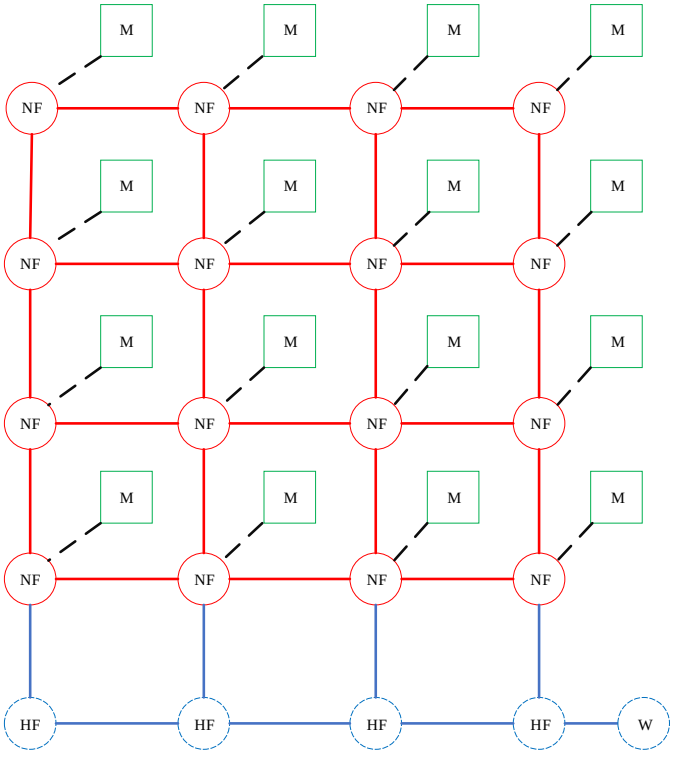

Fig. 2 Schematic illustration of transport between different media.

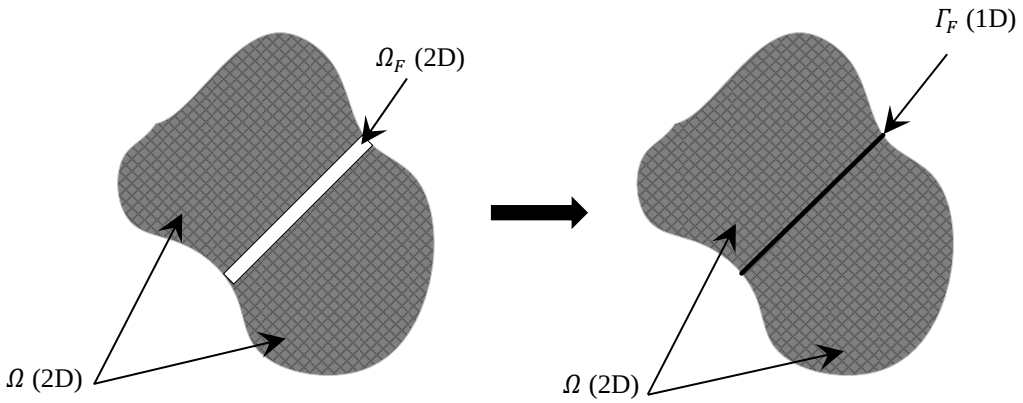

Fig. 3 Schematic representation of the discrete fracture matrix approach.

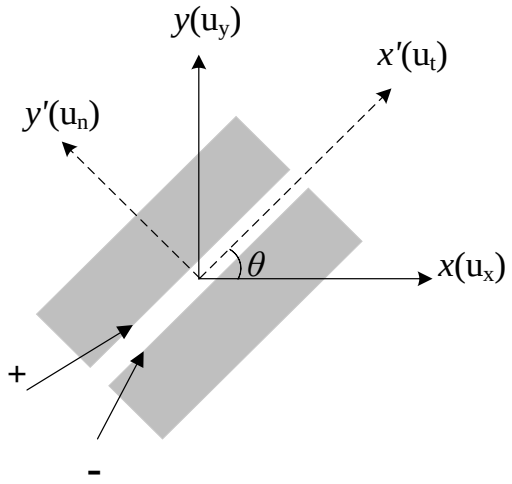

Fig. 4 Transformation between x'-y' local coordinate system (dash) and x-y global coordinate system (solid).

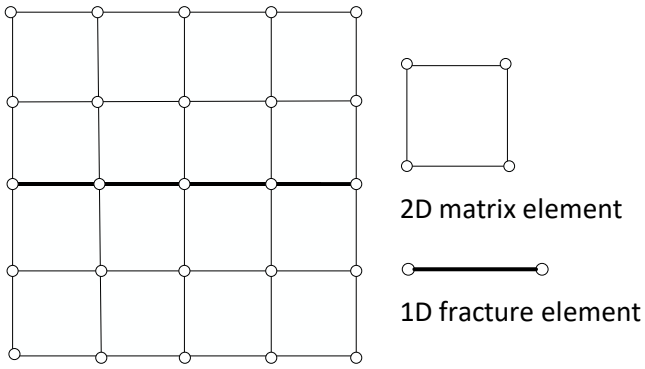

Fig. 5 Mesh for the discrete fractured model: the matrix is discretised using 2D elements and the fracture is discretised using a line element.

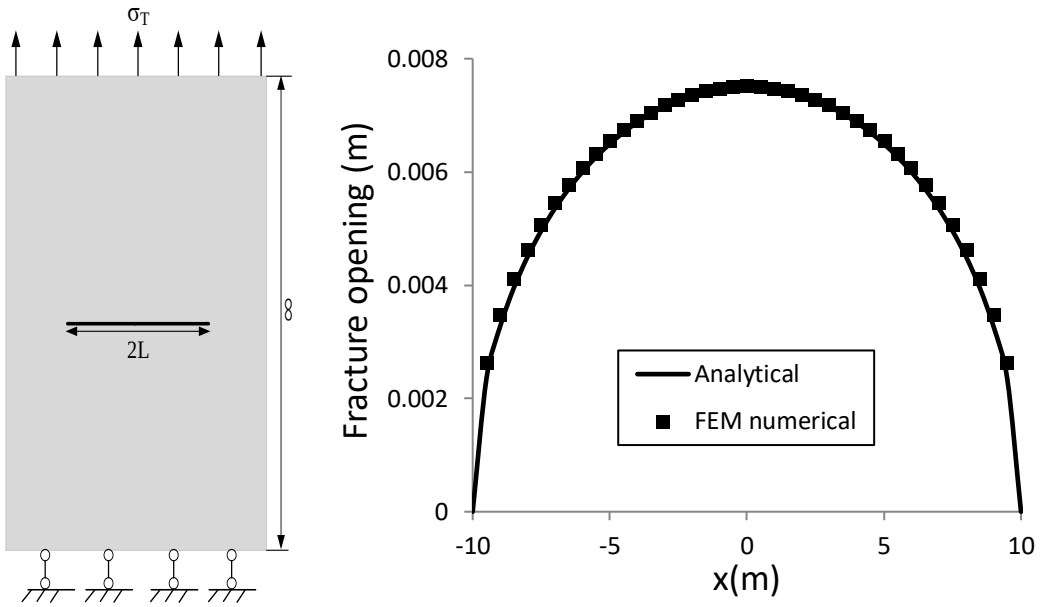

Fig. 6 (a) Plane domain with a central fracture, and (b) a comparison of the numerical results and analytical solution for the fracture opening.

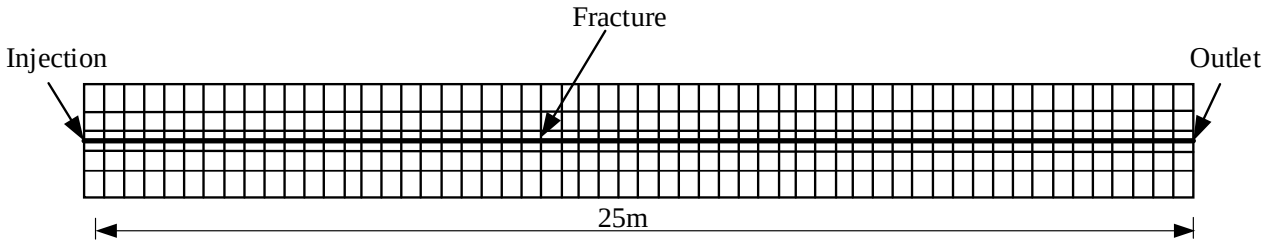

Fig. 7 The geometric configuration used for the analysis of Wijesinghe's problem.

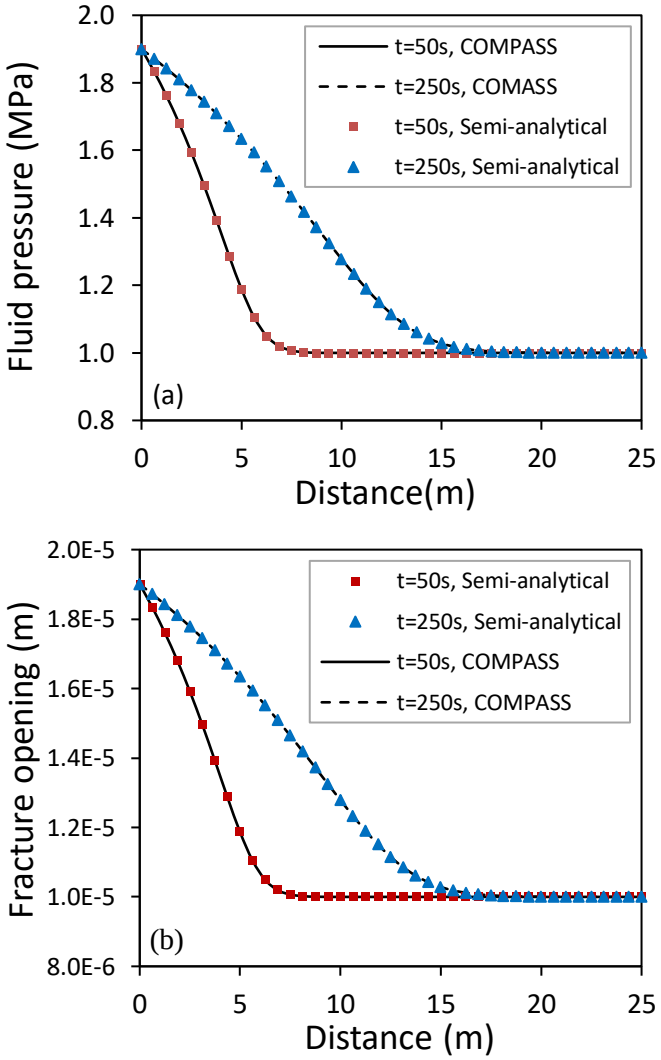

Fig. 8 Comparison of analytical and numerical solutions for (a) fluid pressure and (b) fracture opening.

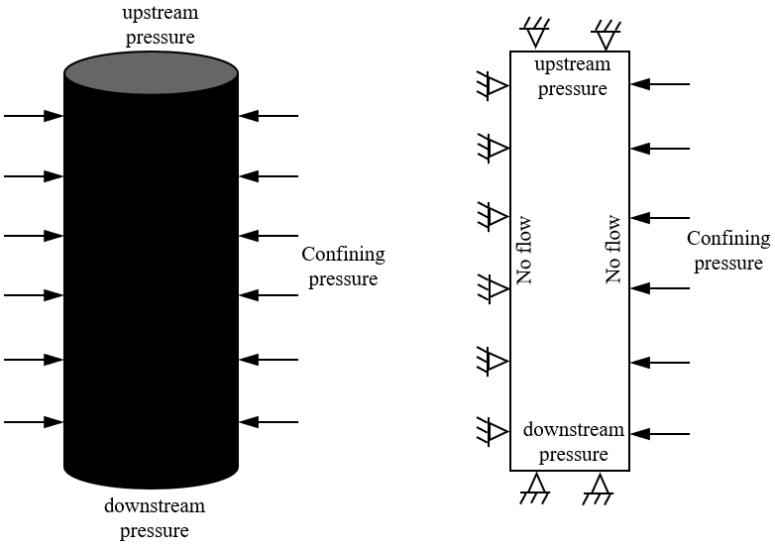

(a) Laboratory coal sample (b) 2D model

Fig. 9 Geometry and boundary conditions of the numerical model under constant confining stress.

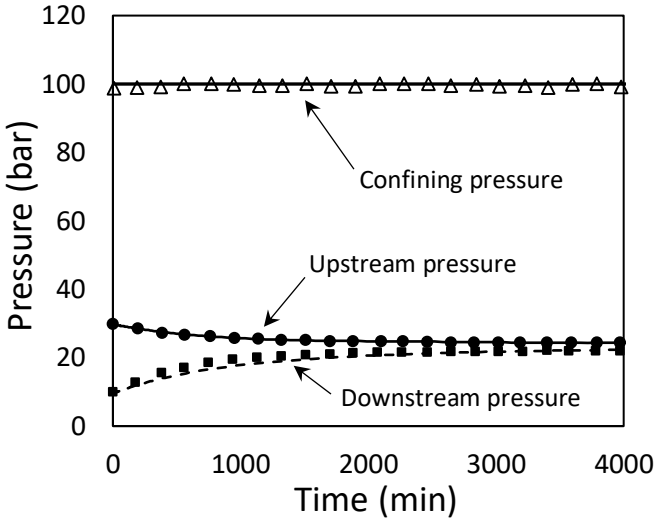

Fig. 10 Comparison of numerical results (lines) and experimental results (symbols) for the upstream pressure and downstream pressure under a constant confining pressure.

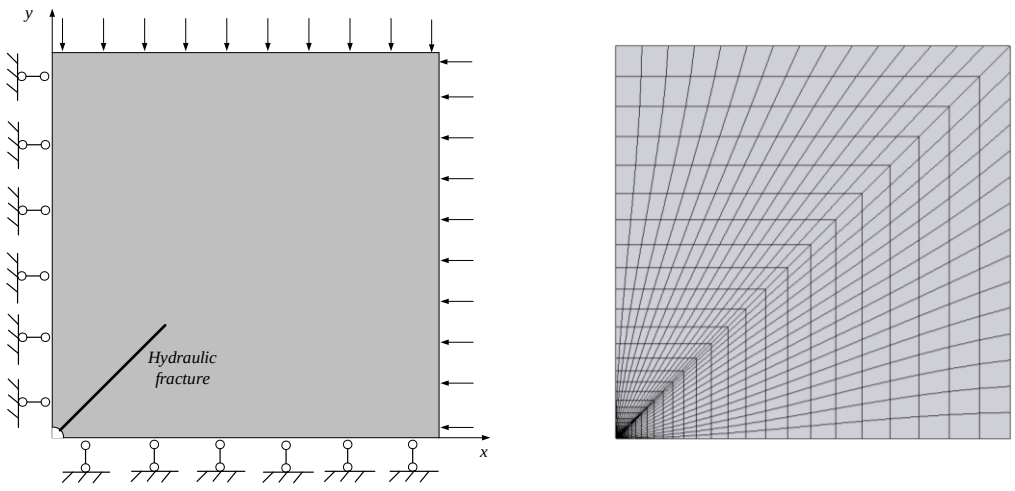

(a) (b)

Fig. 11 (a) Problem domain embedded with a single fracture, showing the assigned boundary conditions, and (b) computational domain showing the mesh geometry.

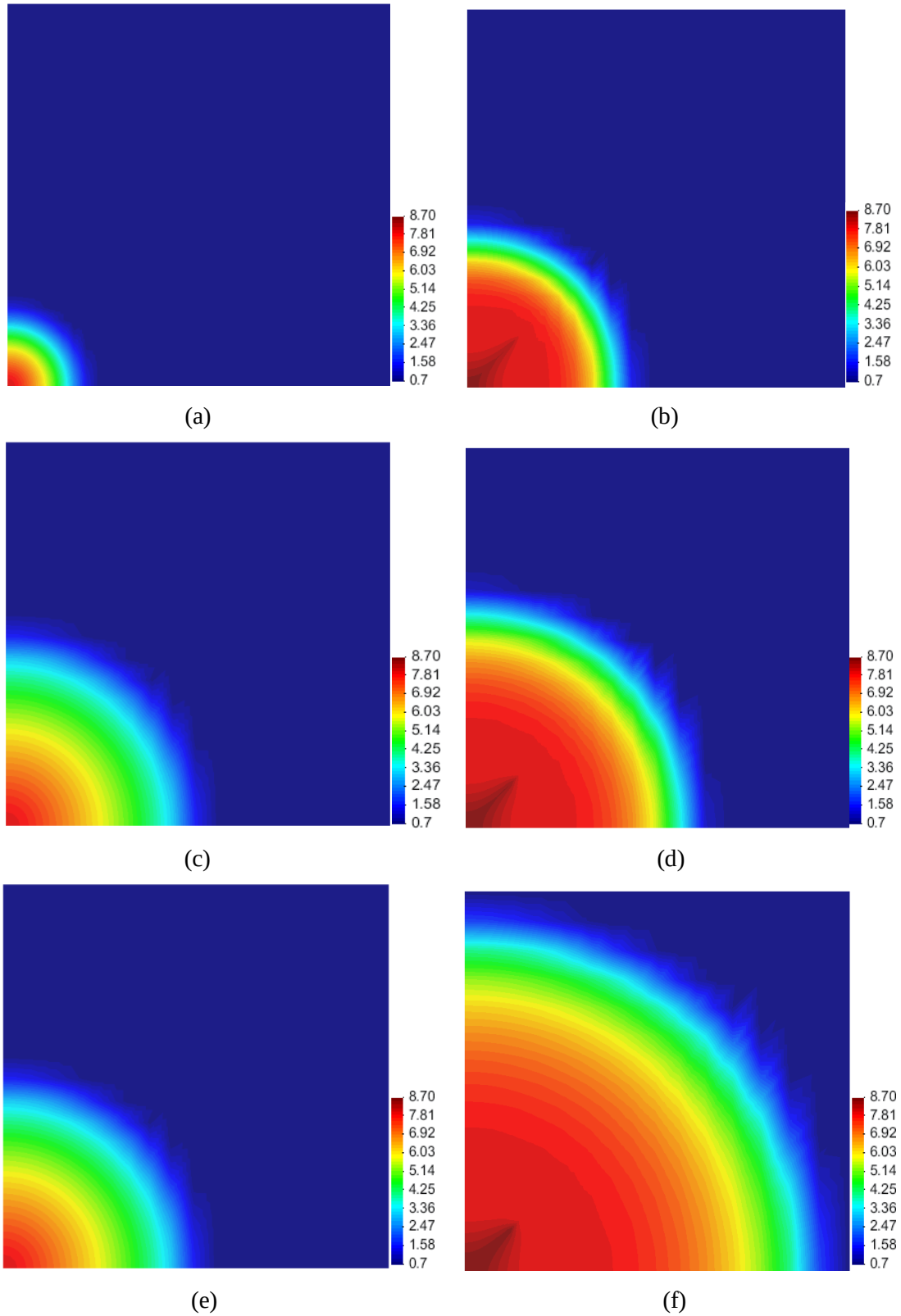

Fig. 12 Distribution of gas pressure outward from the wellbore at different times of 10 days (a, b), 30 days (c, d) and 90 days (e. f), for cases without a hydraulic fracture (a, c, e) and with a hydraulic fracture (b, d, f).

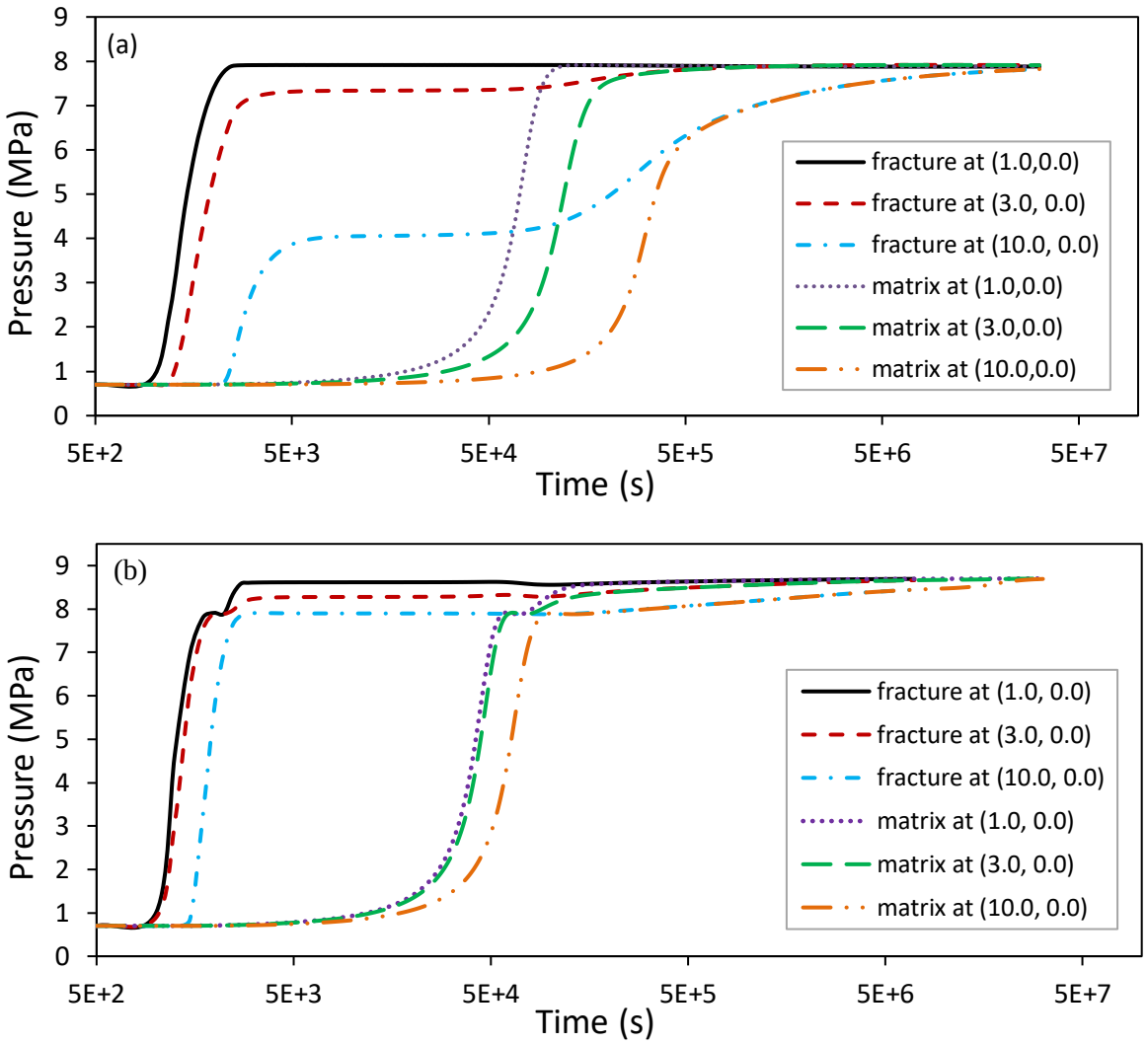

Fig. 13 Evolution of gas pressure with time at specified points, (a) without the hydraulic fracture and (b) with the hydraulic fracture.

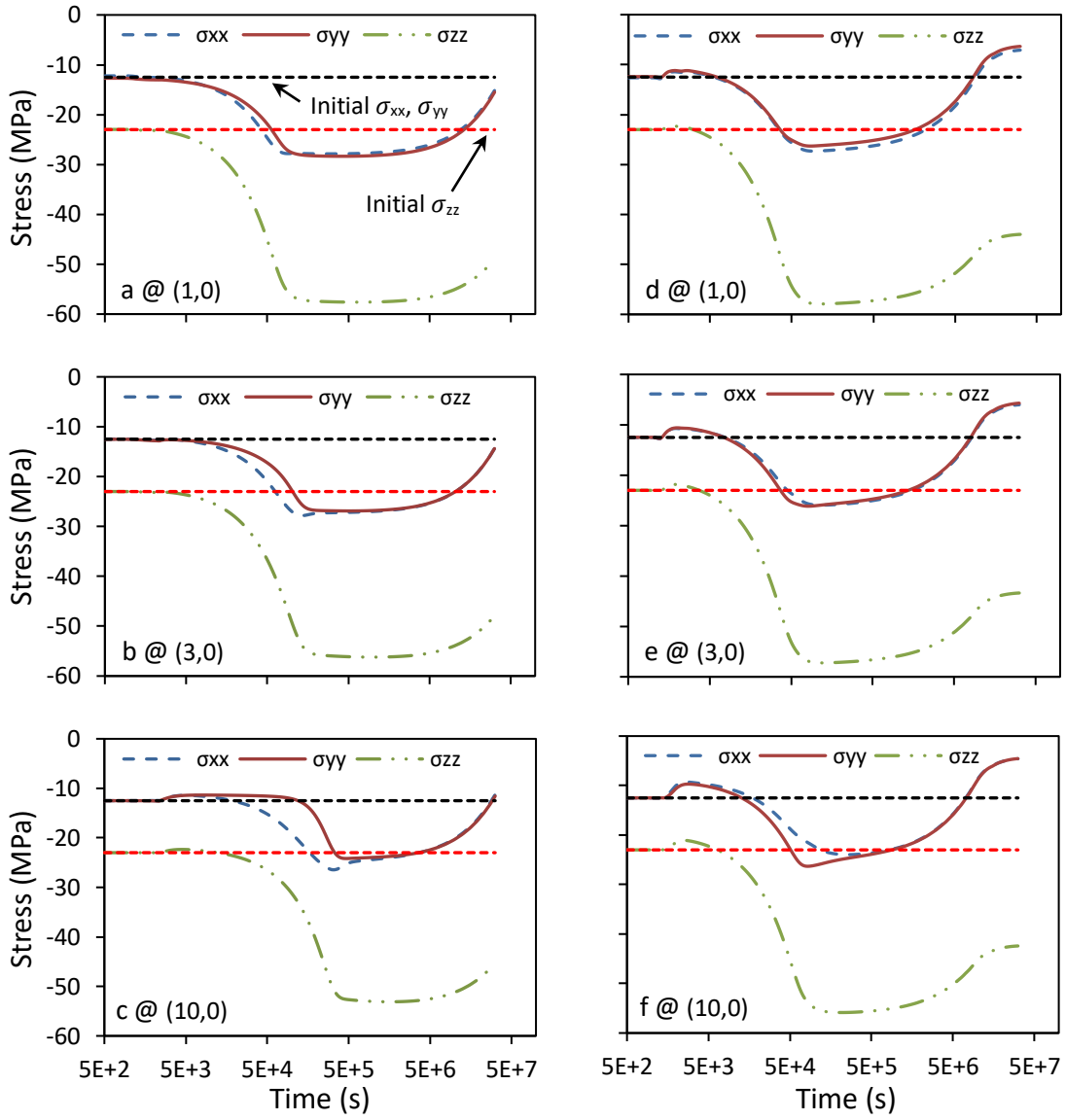

Fig. 14 Changes in horizontal stresses (σ_{xx}, σ_{yy}) and vertical stress (σ_{zz}) with time at the specified points adjacent to the injection well; (a-c) without the hydraulic fracture, and (d-f) with the hydraulic fracture (black and red dashed lines denote the initial horizontal and vertical stress, respectively).

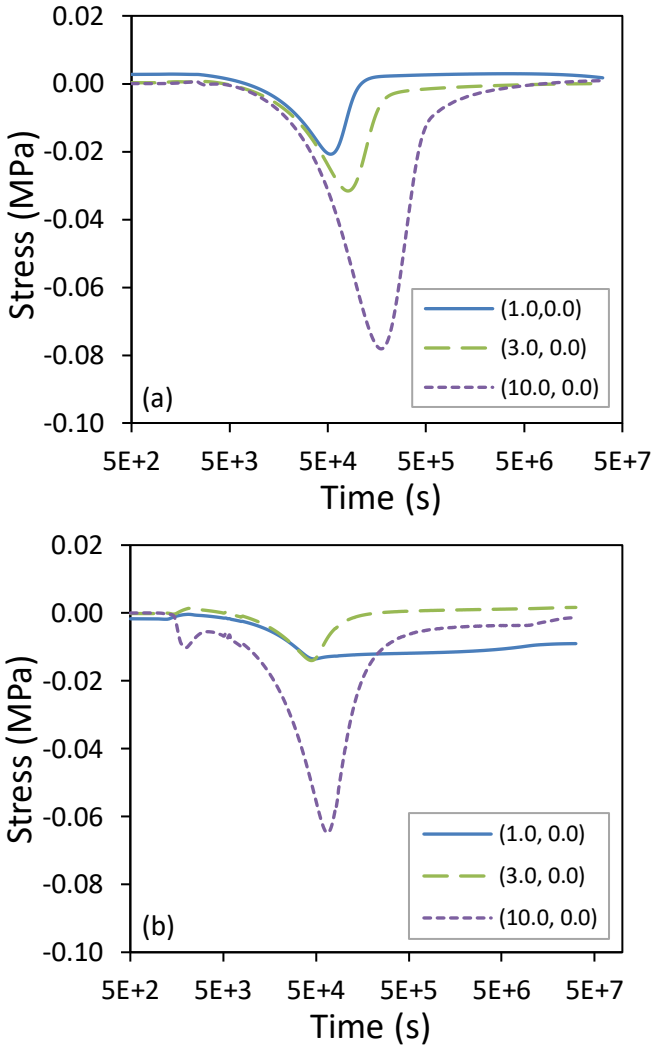

Fig. 15 The evolution of tangential stress (σ_{xy}) with time at specified points adjacent to injection well (a) without hydraulic fracture and (b) with hydraulic fracture.

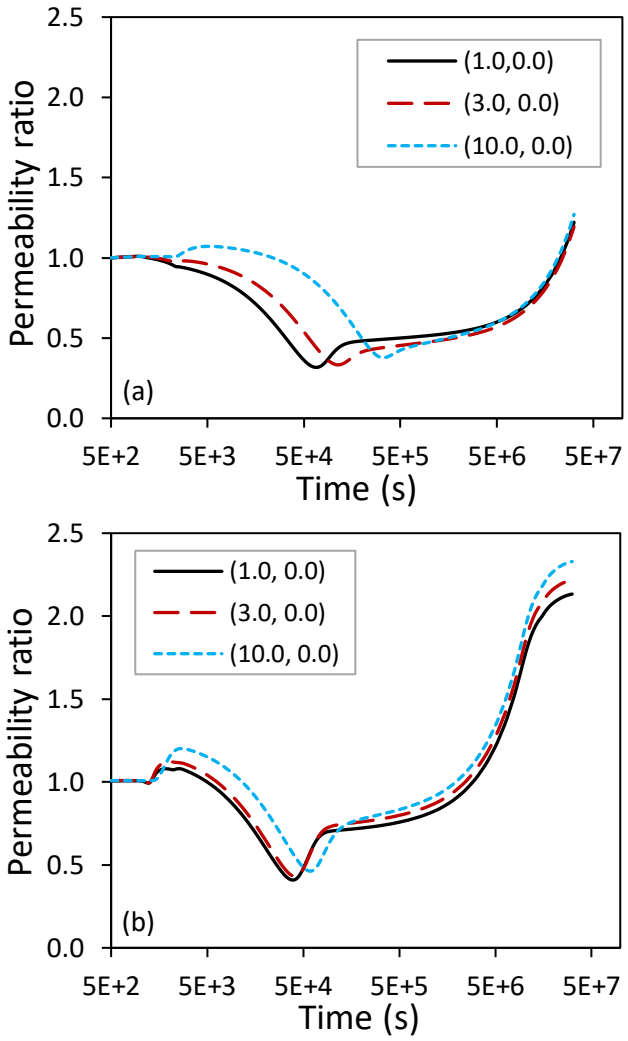

Fig. 16 Evolution of the permeability ratio with time at specified points adjacent to the injection well (a) without the hydraulic fracture, and (b) with the hydraulic fracture.

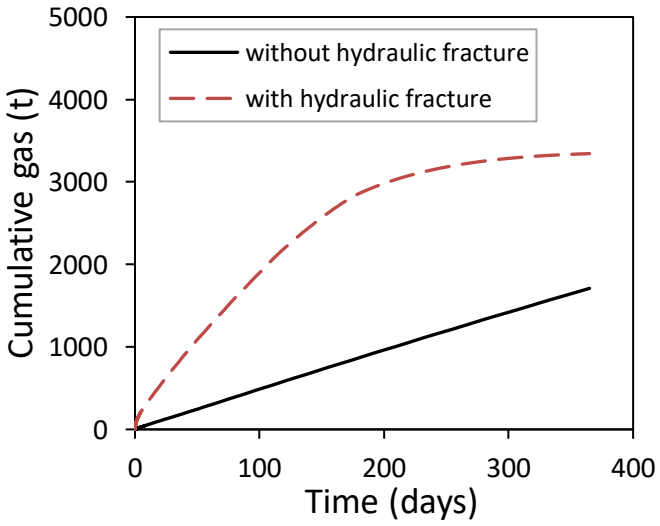

Fig. 17 Comparison of cumulative CO_2 injection between the two simulation scenarios.